Engineering 38 (2024) 164–174

Contents lists available at ScienceDirect

Engineering

journal homepage: www.elsevier.com/locate/eng

Research
Air Pollution Control—Article

A Deep-Learning and Transfer-Learning Hybrid Aerosol Retrieval Algorithm for FY4-AGRI: Development and Verification over Asia

Disong Fu [a], Hongrong Shi [a,b], Christian A. Gueymard [c], Dazhi Yang [d], Yu Zheng [e], Huizheng Che [e,*], Xuehua Fan [a], Xinlei Han [f,g], Lin Gao [h], Jianchun Bian [a,i], Minzheng Duan [a,i], Xiangao Xia [a,i,*]

[a] Key Laboratory of Middle Atmosphere and Global Environment Observation, Institute of Atmospheric Physics, Chinese Academy of Sciences, Beijing 10029, China
[b] Key Laboratory of Cloud-Precipitation Physics and Severe Storms, Institute of Atmospheric Physics, Chinese Academy of Sciences, Beijing 100029, China
[c] Solar Consulting Services, Colebrook, NH 03576, USA
[d] School of Electrical Engineering and Automation, Harbin Institute of Technology, Harbin 150006, China
[e] State Key Laboratory of Severe Weather & Key Laboratory of Atmospheric Chemistry, Institute of Atmospheric Composition and Environmental Meteorology, Chinese Academy of Meteorological Sciences, China Meteorological Administration, Beijing 100081, China
[f] National Institute of Natural Hazards, Ministry of Emergency Management of China, Beijing, 100085, China
[g] Key Laboratory of Compound and Chained Natural Hazards Dynamics, Ministry of Emergency Management of China, Beijing 100085, China
[h] National Satellite Meteorological Center, China Meteorological Administration, Beijing 100081, China
[i] University of Chinese Academy of Sciences, Beijing 100049, China

ARTICLE INFO

Article history:
Received 26 April 2023
Revised 10 July 2023
Accepted 28 September 2023
Available online 10 January 2024

Keywords:
Aerosol optical depth
Retrieval algorithm
Deep learning
Transfer learning
Advanced Geosynchronous Radiation Imager

ABSTRACT

The Advanced Geosynchronous Radiation Imager (AGRI) is a mission-critical instrument for the Fengyun series of satellites. AGRI acquires full-disk images every 15 min and views East Asia every 5 min through 14 spectral bands, enabling the detection of highly variable aerosol optical depth (AOD). Quantitative retrieval of AOD has hitherto been challenging, especially over land. In this study, an AOD retrieval algorithm is proposed that combines deep learning and transfer learning. The algorithm uses core concepts from both the Dark Target (DT) and Deep Blue (DB) algorithms to select features for the machine-learning (ML) algorithm, allowing for AOD retrieval at 550 nm over both dark and bright surfaces. The algorithm consists of two steps: ① A baseline deep neural network (DNN) with skip connections is developed using 10 min Advanced Himawari Imager (AHI) AODs as the target variable, and ② sunphotometer AODs from 89 ground-based stations are used to fine-tune the DNN parameters. Out-of-station validation shows that the retrieved AOD attains high accuracy, characterized by a coefficient of determination (R^2) of 0.70, a mean bias error (MBE) of 0.03, and a percentage of data within the expected error (EE) of 70.7%. A sensitivity study reveals that the top-of-atmosphere reflectance at 650 and 470 nm, as well as the surface reflectance at 650 nm, are the two largest sources of uncertainty impacting the retrieval. In a case study of monitoring an extreme aerosol event, the AGRI AOD is found to be able to capture the detailed temporal evolution of the event. This work demonstrates the superiority of the transfer-learning technique in satellite AOD retrievals and the applicability of the retrieved AGRI AOD in monitoring extreme pollution events.

© 2024 THE AUTHORS. Published by Elsevier LTD on behalf of Chinese Academy of Engineering and Higher Education Press Limited Company. This is an open access article under the CC BY-NC-ND license (http://creativecommons.org/licenses/by-nc-nd/4.0/).

1. Introduction

Detailed information on aerosols is essential for a broad range of geoscience domains, such as the Earth's radiation balance [1,2], climate change [3], air quality [4,5], and human health [6], to name just a few. Aerosol optical depth (AOD), which is defined as the vertical integral of the extinction coefficient of atmospheric aerosols from the ground to the top of the atmosphere (TOA), is a widely used and essential optical parameter for characterizing atmospheric aerosols. In parallel, ground-based sunphotometer remote sensing is widely regarded as the most accurate method for obtaining AOD. Sunphotometer AODs are thus often used as ground truth to validate a wide variety of aerosol products from satellite remote sensing, chemical transport models, and

* Corresponding authors.
E-mail addresses: chehz@cma.gov.cn (H. Che), xxa@mail.iap.ac.cn (X. Xia).

https://doi.org/10.1016/j.eng.2023.09.023
2095-8099/© 2024 THE AUTHORS. Published by Elsevier LTD on behalf of Chinese Academy of Engineering and Higher Education Press Limited Company.
This is an open access article under the CC BY-NC-ND license (http://creativecommons.org/licenses/by-nc-nd/4.0/).

atmospheric reanalysis [7–11]. Development of the Aerosol Robotic Network (AERONET) began more than 25 years ago, and the network has grown to include hundreds of sunphotometric stations worldwide [12,13]. There are also a few regional sunphotometer networks in Asia, such as the SKY radiometer NETwork (SKYNET) [14]. In China, three independent sunphotometer networks—namely, the Chinese Aerosol Research Network (CARSNET) [15], the Chinese Sun Hazemeter Network now known as the Campaign on Atmospheric Aerosol Research network of China (CARE-China) [16], and the Sun–Sky Radiometer Observation Network (SONET) [17]—have been established to meet the increasing demand for research-grade aerosol data. In addition, a few stations from the international AERONET and SKYNET networks operate throughout China. All these networks play a vital role in characterizing aerosol properties over China. However, the high spatiotemporal variability of aerosols cannot be fully captured by these sparsely distributed sunphotometer instruments. Hence, satellite remote sensing is greatly needed to provide AOD products with high spatiotemporal coverage.

Satellite remote sensing, which mainly refers to the sensing provided by polar-orbiting and geostationary satellites, has been ubiquitously used to acquire aerosol properties spatiotemporally. Polar orbiting satellites can detect global AOD but have relatively long revisit periods. In comparison, geostationary satellites have the advantage of providing high-frequency aerosol observations (about 5–15 min) at good spatial resolutions. Current sensors of that kind include: the Spinning Enhanced Visible and Infrared Imager onboard Meteosat Second Generation from the European Organization for the Exploitation of Meteorological Satellites [18]; the Advanced Baseline Imager (ABI) of Geostationary Operational Environmental Satellites (GOES)-16/17[†] from the National Oceanic and Atmospheric Administration (NOAA); the Advanced Himawari Imager (AHI) onboard Himawari-8 and its successor[‡], Himawari-9, from the Japan Meteorological Agency [19]; and the Geostationary Ocean Color Imager II (GOCI-II) of the Geostationary Korea Multi-Purpose Satellite 2B (GEO-KOMPSAT-2B) [20]. Fig. S1 in Appendix A presents the positions and coverages of the six geostationary satellites that cover China wholly or partially—namely, Meteosat-9 (also known as the Indian Ocean Data Coverage, IODC) at 45.5°E, Himawari-8/9 at 140.7°E, GEO-KOMPSAT-2B at 128°E, Fengyun-4A (FY-4A) at 104.7°E, and Fengyun-4B (FY-4B) at 133°E. Although Himawari-8/9 and IODC cover parts of China, none of these satellites can provide data for the entire country with a good field of view. In contrast, FY-4A and FY-4B can now provide full coverage and high-frequency measurements over China and neighboring countries [21]. These respectively constitute the first and second instance of the new generation of Chinese geostationary meteorological satellites. Both satellites carry various instruments, including the Advanced Geosynchronous Radiation Imager (AGRI) sensor, which is central to the present study and whose capabilities have been reviewed by Zhang et al. [22].

The most challenging task in passive satellite AOD retrieval over land is to separate the surface and aerosol contributions from the reflected radiance that is sensed by spaceborne radiometers. This is especially true when the surface is highly reflective (e.g., snow or bright sand) and the AOD signal is low. To address this problem, researchers have developed various physical schemes, which can be divided into four main categories: ① the establishment of surface reflectance relationships between the visible and other bands, such as the Dark Target (DT) method [23]; ② the construction of a pre-calculated static surface reflectance database, with the Deep Blue (DB) and the enhanced DB algorithm [24–26] as typical examples; ③ the use of a multi-angle method, as represented by the multi-angle implementation of atmospheric correction (MAIAC) [27]; and ④ the use of polarization information, such as the usage of the Generalized Retrieval of Aerosol and Surface Properties unified algorithm in Polarization and Directionality of the Earth's Reflectances [28]. Attempts have already been made to use the above algorithms for AOD retrieval from geostationary satellites. For example, the NOAA GOES-16 ABI AOD over land uses a DT-based method [29]. In contrast, the operational AHI land aerosol product, released by the Japan Aerospace Exploration Agency, uses a DB-type method, where the second lowest reflectance measurement in a month is atmospherically corrected to represent the surface reflectance [30].

Benefiting from the advancement of computer technology, machine-learning (ML) has rapidly gained great interest within the remote-sensing field. Critically, ML can help model the complex relationship between satellite-observed TOA reflectance and surface-based AOD. She et al. [31] utilized a deep neural network (DNN) model to estimate AOD from AHI, with AOD data from 76 AERONET sites serving as the ground truth. The root mean-squared error (RMSE) achieved by their model was 0.17, demonstrating its effectiveness in AOD estimation. Yeom et al. [32] employed DNN in a similar way but focused on the GOCI sensor and AERONET AOD data over Northeast Asia. Their validation results exhibited high accuracy for the DNN-generated AOD when compared with either traditional support vector regression or random forest (RF) models. In contrast to previous works, Kang et al. [33] introduced channel difference features into a DNN model, indirectly incorporating surface reflectance information. The coefficient of determination (R^2) of ten fold cross-validation reached 0.93 and 0.92 for a light gradient boosting machine and RF, respectively. Chen et al. [34] directly utilized surface reflectance data derived from the Moderate Resolution Imaging Spectroradiometer (MODIS) alongside ground-measured AOD to train a convolutional neural network model. The evaluation demonstrated that approximately 68% of the AOD values fell within the expected error (EE) range of ±(0.05 + 15%). It should be emphasized that, even though these studies employed different sensors, methods, and input features, they all relied solely upon ground observations, which are sampled very sparsely with respect to the area over which the retrieval is required.

Whereas the abovementioned literature leverages observations from AHI, GOCI, and MODIS, there is no operational AOD product from AGRI yet, although some attempts have been made. For example, Jiang et al. [35] developed an algorithm for retrieving AGRI AOD over land. This algorithm uses a monthly surface reflectance band-ratio database and look-up tables (LUTs) computed by the Second Simulation of a Satellite Signal in the Solar Spectrum Vector model to retrieve hourly AOD. The accuracy was reported to be fairly high, with an R^2 of 0.71, RMSE of 0.16, and approximately 60% of the retrieved AODs within the EE. Xie et al. [36] developed a multi-channel (MC) algorithm for AGRI over South Asia. This algorithm assumes that the relationships between the surface reflectance in different bands remain stable over a period of two weeks. The surface reflectance is derived when aerosol loading is low and MODIS AOD is used for atmospheric correction. The MC algorithm is claimed to be applicable to both dark targets and bright surfaces. In comparison with AERONET AODs, the MC-retrieved AGRI AOD shows high accuracy, with the RMSE and EE of the data being 0.16 and 63.71%, respectively. Ding et al. [37] recently applied the so-called Neural Network AEROsol Retrieval for Geostationary Satellite (NNAeroG) to the full-disk area of AGRI. The AOD data from 111 sunphotometer sites (AERONET + SONET) were used to train the network, and 28 other sites were reserved for independent validation. The AGRI AOD predicted by NNAeroG

[†] Collectively known as "GOES-R" series.

[‡] Himawari-9 became Japan Meteorological Agency's operational satellite on December 13, 2022, replacing Himawari-8, which was then placed in standby mode.

was found to be consistent with the sunphotometer AOD data (RMSE = 0.24, R^2 = 0.73, EE = 58.7%).

To summarize the advances in satellite AOD retrieval, physical retrieval methods (e.g., DT or DB) usually require prior knowledge of aerosol properties, except for the unknown AOD over the area of interest. A radiative transfer model is run to build a LUT for subsequent AOD retrievals. However, the size of the LUT grows exponentially with predefined parameters, and the LUT is usually unique for each sensor. This means that it is difficult to adapt physical retrieval methods to new contexts. In addition, the rapid development of installed sunphotometer stations is not fully exploited by physical retrieval methods, because these stations are used only to characterize aerosol properties or as verification references. In connection with the abovementioned ML-based AOD algorithms, only sunphotometer-based AODs have been used as targets so far. One notable pitfall of this approach is that ground-based stations are still relatively scarce and unevenly distributed, which inevitably lowers the confidence in AOD retrieval over areas that are not covered by at least a few stations. Considering the high heterogeneity of aerosol and surface properties, it seems very improbable that ML models based on limited training samples can be universal.

Given these problems, the goal of this contribution is to develop a novel AGRI AOD retrieval algorithm using both deep-learning and transfer-learning techniques. This innovation includes the following three aspects. First, the features of the ML model are selected based on the core physical concepts of the DT and DB algorithms. Second, a transfer-learning technique is used to overcome the limitation of training samples. This involves training a model by using the AHI AOD as a target whose parameters are tuned by using as many sunphotometer measurements as possible. Since AHI AODs are used in the process, this algorithm enables synergy between a physical retrieval algorithm and an ML method. Finally, a detailed sensitivity analysis is performed to discuss potential sources of error.

2. Data and methods

2.1. AGRI sensor

FY-4A was launched on December 11, 2016, and remains positioned at a longitude of 104.7°E. It is the first of China's latest-generation geostationary meteorological satellites [21,38]. Compared with the instruments that equipped the first generation of Chinese geostationary satellites (FY-2), the AGRI onboard FY-4A has significant improvements in several aspects. First, the number of spectral bands is increased from 5 to 14, providing more refined spectral information. Second, the snapshot interval for the full-disk Earth-view images is reduced from 30 to 15 min, while the Central and Eastern Asia regions are observed every 5 min. This high temporal resolution can help capture high-frequency variations in the observed processes. Third, AGRI has a higher spatial resolution: 1 km in the visible, 2 km in the near-infrared (IR), and 4 km in the other IR spectral bands. This facilitates the analysis of small-scale spatial variations, which is vital to the understanding of the local aerosols' characteristics and transport mechanism.

For this study, a subset of the AGRI/FY-4A Level 1 (L1) 4 km dataset with 5 min temporal resolution was obtained from the FENGYUN Satellite Data Center[†], spanning the full year of 2018. The cosines of the satellite view zenith angle (CSVA) and solar zenith angle (CSZA), seven bands of AGRI (470, 650, 825, 1375, 1610, 2250 nm, and 10.7 μm), as well as a few quantities obtained by combining different bands, are taken as features during the ML model development (details are provided in Section 3). The links of datasets used in this study and the retrieved AGRI AOD are provided in Supplementary Text in Appendix A.

2.2. AHI AOD from Himawari-8

The AHI radiometer on Himawari-8/9 is equipped with 16 channels, with a spatial resolution of 0.5–2 km and a temporal resolution of 10 min [19]. An optimal estimation algorithm was developed to simultaneously retrieve the AOD, single scattering albedo at 500 nm, and Ångström exponent (AE) at 400–600 nm [30]. Over land, the algorithm assumes that the surface reflectance remains unchanged in a month; the second minimum reflectance on an hourly scale is selected to establish the surface reflectance database. Over oceans, the sea surface reflectance is calculated based on the Cox and Munk method [39]. In this study, the Version 3 L2 AOD retrievals with either "very good" or "good" quality at 10 min resolution are used to train a baseline model (details are provided in Section 3). Eq. (1) is used to obtain the AOD at 550 nm using AHI's AE and AOD at 500 nm:

$$\tau_{550} = \tau_{500} \times (550/500)^{-\mathrm{AE}} \quad (1)$$

where τ_{550} and τ_{500} are the AODs at 550 and 500 nm, respectively.

2.3. Sunphotometer AOD

In the transfer learning, ground-based sunphotometer aerosol products are used as a reference to fine-tune the baseline model. Both AERONET and CARSNET AOD products are used here. CARSNET is a ground-based aerosol monitoring system established by the China Meteorological Administration (CMA). CARSNET sunphotometers are calibrated annually according to a stringent calibration protocol, resulting in AOD measurements with the same accuracy as those from AERONET [15]. AOD data at 89 stations over Asia (CARSNET + AERONET) are used in this study (Fig. S2 in Appendix A). To the best of our knowledge, this is by far the largest number of stations with sunphotometer data ever reported in the literature for that part of Asia. The AOD at 550 nm is simply interpolated from its counterparts at 440, 675, 870, and 1020 nm, using the interpolation method described in Ref. [11].

2.4. Auxiliary data

The auxiliary data include hourly meteorological quantities derived from the fifth generation European Centre for Medium-Range Weather Forecasts (ECMWF) atmospheric reanalysis (ERA5) produced at a spatial resolution of 0.25° × 0.25° [40]. These quantities are 2 m temperature (T2M, K), total columnar water vapor (PWV, kg·m^{-2}), total columnar ozone (O_3, kg·m^{-2}), boundary layer height (BLH, m), and surface pressure (SP, Pa). Elevation (ELV, m) from the shuttle radar topography mission's digital elevation model (DEM) with a 90 m spatial resolution is used as a predictor to explain the AOD's elevation dependence. A coarse time variable (T)—namely, the day of the year—is used to reflect the seasonality of AOD; it is encoded as $\cos(2\pi \times T/365)$. Finally, since previous studies have shown that the satellite-derived AOD uncertainty varies with surface types [41], the land-cover types obtained from the MODIS Land Cover Climate Modeling Grid (MCD12C1) version 6 product [42] are also used as a feature.

3. Retrieval methodology

The uncertainty in satellite aerosol retrievals comes from four major sources: sensor calibration, cloud detection, aerosol model selection, and surface reflectance determination [43,44]. Here, much attention is given to cloud detection, surface reflectance

[†] http://data.nsmc.org.cn.

estimation, and aerosol retrieval strategy. AGRI's calibration accuracy is 5% for reflective solar bands [21], which will be discussed in Subsection 4.4, along with the sensitivity analysis.

3.1. Cloud/snow/ice/water pixel mask

For the following aerosol retrievals, a simple but robust cloud detection algorithm is first developed with reference to the work of Su et al. [44] and the GOES-R ABI Algorithm Theoretical Basis Document [29]. The detection algorithm consists of a set of thresholds and tests, including a reflectance and brightness temperature threshold test, a brightness temperature difference and spatial inhomogeneity test, and a water and snow/ice pixel identification (Table 1). The key variables are the TOA reflectances (R_λ), at wavelengths (λ) of 470, 510, 640, 650, 825, 860, 1375, 1610, and 2250 nm, as well as the brightness temperatures (BT_λ), at λ = 8.5 and 10.7 μm.

3.2. Estimation of surface reflectance proxy

Precise discrimination between surface reflectance and aerosol backscattering is critical for accurate AOD retrieval and has often not been carefully considered in previous ML-based algorithms [31,32,45]. To address this potential problem, this study adopts the DB method to create a dynamic hourly database of surface reflectance at 470, 650, and 2250 nm (noted ρ_{470}, ρ_{650}, and ρ_{2250}, respectively) for each month. All AGRI measurements that are free of both clouds and snow/ice are retained. Considering that, every 3 h, AGRI makes two full disk scans during the first 30 min and six regional scans every 5 min for the remaining 30 min, there are at least 168 regional scans per month for a single hour. Because satellite reflectance measurements are dominated by the surface reflectance when the aerosol loading is low, and because aerosols generally enhance the reflectance measurement, the second lowest hourly TOA reflectance for each pixel in a month is selected here to represent the hourly surface reflectance. It is emphasized that the bidirectional property of surface reflectance is taken into account. As an example, the left and right panels of Fig. S3 in Appendix A show the baseline values of ρ_{470}, ρ_{650}, and ρ_{2250} in May and October, respectively. It should be noted that the missing values in some grids are filled using nearest-neighbor interpolation. The spatial distribution of surface reflectance is consistent across the three bands, with the lower values found in southern China and the higher values in the north, west, and northwest of the domain.

Table 1
Criteria for the cloud/snow/ice/water pixel masks in this study.

Classes	Criteria
Over land	
Dense cloud	R_{470} > 0.3
Cloud	Brightness temperature at 10.7 μm ($BT_{10.7}$) < 260 K
Edges of cloud	Standard deviation calculated from 3 × 3 pixels at R_{470} > 0.02 and standard deviation calculated from 3 × 3 pixels at $BT_{10.7}$ > 4.5 K
Cirrus cloud	$BT_{8.5}$–$BT_{10.7}$ > 1.0 K or R_{1375} > 0.018
Water	Normalized difference water index (NDWI) > 0.2
Snow	Normalized difference snow/ice index (NDSI) > 0.3 and not water or cloud
Over ocean	
Dense cloud	R_{860} > 0.3
Cirrus cloud	R_{1375} > 0.018
Edges of cloud	Standard deviation calculated from 3 × 3 pixels at R_{2250} > 0.008
Ice	NDSI > 0.3, R_{640} > 0.2, R_{860} > 0.17, and $BT_{10.7}$ < 275 K

NDWI: difference between R_{510} and R_{860} normalized by the sum of R_{650} and R_{825}; NDSI: difference between R_{825} and R_{1610} normalized by the sum of R_{825} and R_{1610} [25].

Based on the two exemplary months shown, seasonal variations in surface reflectance are also evident. These results suggest that the second lowest hourly TOA reflectance can effectively be considered as a proxy for surface reflectance, considering that no atmospheric correction can be applied at that stage. Atmospheric correction requires accurate AOD (which is generally not available) as well as radiative transfer model simulations [36,46], which would considerably increase the method's complexity. Using the second lowest hourly TOA reflectance simplifies the algorithm because no external data is required.

3.3. ML AOD retrieval model development

Fig. 1 illustrates the overall framework of the retrieval algorithm, which consists of three submodules: ① data preprocessing (orange box); ② baseline model tasks (green box); and ③ transfer-learning tasks (blue box). The data stream from multiple sources with different spatiotemporal resolutions is processed into a unified resolution of 4 km. Then, a baseline model (DNN with skip connections) is developed for the initial AOD estimation by using the AHI AOD as target. Finally, the baseline model is improved by the transfer-learning scheme using the sunphotometer AOD as the target. The whole procedure can thus be summarized as "preprocessing + DNN + fine-tuning."

3.3.1. Data preprocessing

The temporal and spatial resolutions of the original sources are summarized in Table 2 [25]. The spatial resolution of all datasets is re-gridded to 4 km via linear interpolation. The variables of the ERA5 reanalysis are assumed to remain constant within each hour. Thus, the ERA5 outputs closest to the AGRI observation time are used as the auxiliary variables. For hybrid deep learning and transfer learning, two models need to be trained sequentially. Thus, the input data in Table 2 needs to be matched with both the AHI AOD and sunphotometer AOD, respectively, although the two sets of training-target locations need not coincide. For the AHI AOD, 900 sampling points are nearly uniformly selected from the Himawari-8 domain according to the MCD12C1 land types (i.e., about 60 points for each land type). The AHI AOD over these 900 sampling points for each observation in 2018 is extracted as the target for the training of the baseline model. The input datasets within ±2.5 min of the AHI observation time over these points are also extracted to match the AHI AOD L2 products. The matching of the sunphotometer AOD is the same as for the AHI AOD, except for the actual site locations. After data matching, the total number of AHI and sunphotometer AOD samples are 1 156 090 and 127 794, respectively. A standard normalization is applied to the input data, which standardizes the features by subtracting the mean and scaling to unit variance. The logarithmic transformation is applied to the target variable, since it is standard practice to transform the typically lognormal AOD distribution into an approximately normal distribution.

3.3.2. Baseline model

A schematic diagram of the baseline model architecture is depicted in Fig. 2. The DNN is constructed by extending the "shallow" network (i.e., an ANN with an input layer, one hidden layer, and an output layer) to multiple hidden layers [47]. In this study, a total of 16 predictors are fed into both the input layer (orange part in Fig. 2) and the 550 nm AHI AOD (the red node in the figure) as the output layer, using four hidden layers. It should be noted that, although there are five gray blocks in the figure, the output from a block is a part of the input of the next block. The batch normalization, the rectified linear unit (ReLU) activation layer, and the dropout mechanism are integrated into the processing cell (green rectangle in Fig. 2) to regularize the network, add nonlinearity,

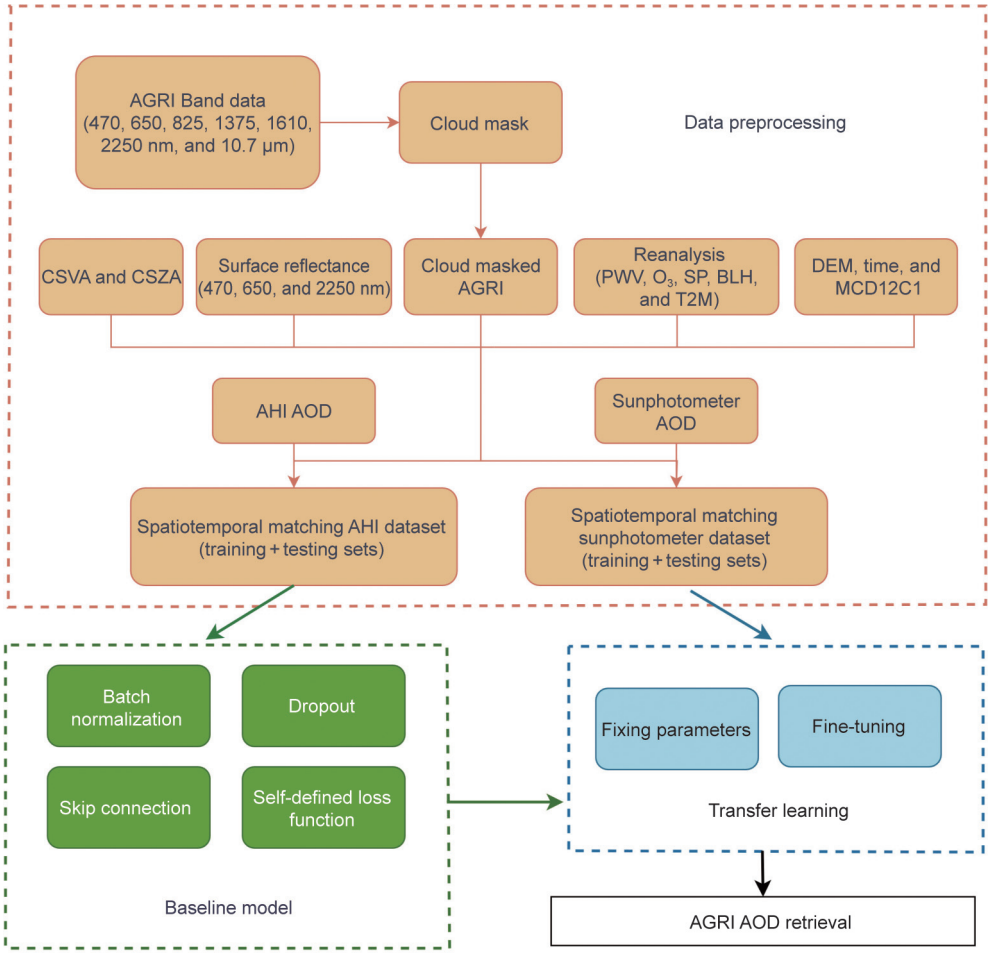

Fig. 1. Flowchart of the deep-learning and transfer-learning hybrid method for AGRI AOD retrieval.

Table 2
Summary of input features for the proposed retrieval algorithm [25].

Input source	Variables	Spatial resolution	Temporal resolution
FY4A/AGRI	R_{470}, R_{650}, R_{2250}, CSVA, CSZA	4 km	5 min
Reanalysis	T2M, PWV, O_3, SP, BLH	0.25°	1 h
Surface reflectance	ρ_{470}, ρ_{650}, ρ_{2250}	4 km	5 min
Geographic information	ELV	90 m	Yearly
Land cover types	MCD12C1	5 km	Yearly
T variable	*T* (day of year)	4 km	5 min

and reduce overfitting, respectively. In addition, the skip connection (represented by the red lines in the figure) is adopted to improve the DNN and to prevent the gradient from vanishing [48–50].

In parallel, state-of-the-art practices for DNN training are used here. The mini-batch gradient descent search method is used with 60 epochs and a batch size of 512 to ensure a stable and robust solution. The learning rate is initialized as 0.01 and decreases to 0.001 and 0.0001 at the 20th and 40th epochs, respectively. The Adam optimizer is selected because it can converge quickly and stably [51]. Although the target variable (i.e., AOD) is logarithmic, it is still an imbalanced dataset characterized by a long tail to very large values. Studies have indicated that the mean-squared error (MSE) loss would underestimate the most infrequent data points in imbalanced regression problems [52,53]. Therefore, a special loss function (Eq. (2)) is designed to compensate for the underestimation of large AODs. It stipulates that if the prediction value $\hat{y}_n$ is larger than the target value y_n, the Loss is equal to half of the MSE; otherwise, the Loss is exactly equal to the MSE:

$$\text{Loss}_n = \begin{cases} 0.5(y_n - \hat{y}_n)^2, & \text{if } y_n - \hat{y}_n < 0 \\ (y_n - \hat{y}_n)^2, & \text{otherwise} \end{cases} \quad (2)$$

3.3.3. Transfer learning

Even if the DNN model can accurately reproduce the AHI AOD at 550 nm, the prediction still has a certain degree of uncertainty as compared with ground-based sunphotometer products. This is to be expected because the AHI 550 nm AOD uncertainty is not negligible [54,55]. To further improve prediction accuracy, an additional step of transfer learning is employed.

Transfer learning is a powerful technique that has been used to achieve state-of-the-art results in many domains [56]. For example, Liu et al. [57] transferred a precipitation fusion model from the source domain to the target domain. As a result, the RMSE and MSE of the precipitation predictions in the Qinghai–Xizang Plateau were significantly reduced (by 27.6% and 22.5%, respectively) after fine-tuning.

In general, the first layer of the pretrained network is not particularly related to the target dataset, unlike the last layer of the network, which is closely related to the target task. Correspondingly, the features of the first layer are called "general features," whereas those of the last layer are called "specific features." Therefore, the fine-tuning strategy usually adjusts the parameters of the last full-

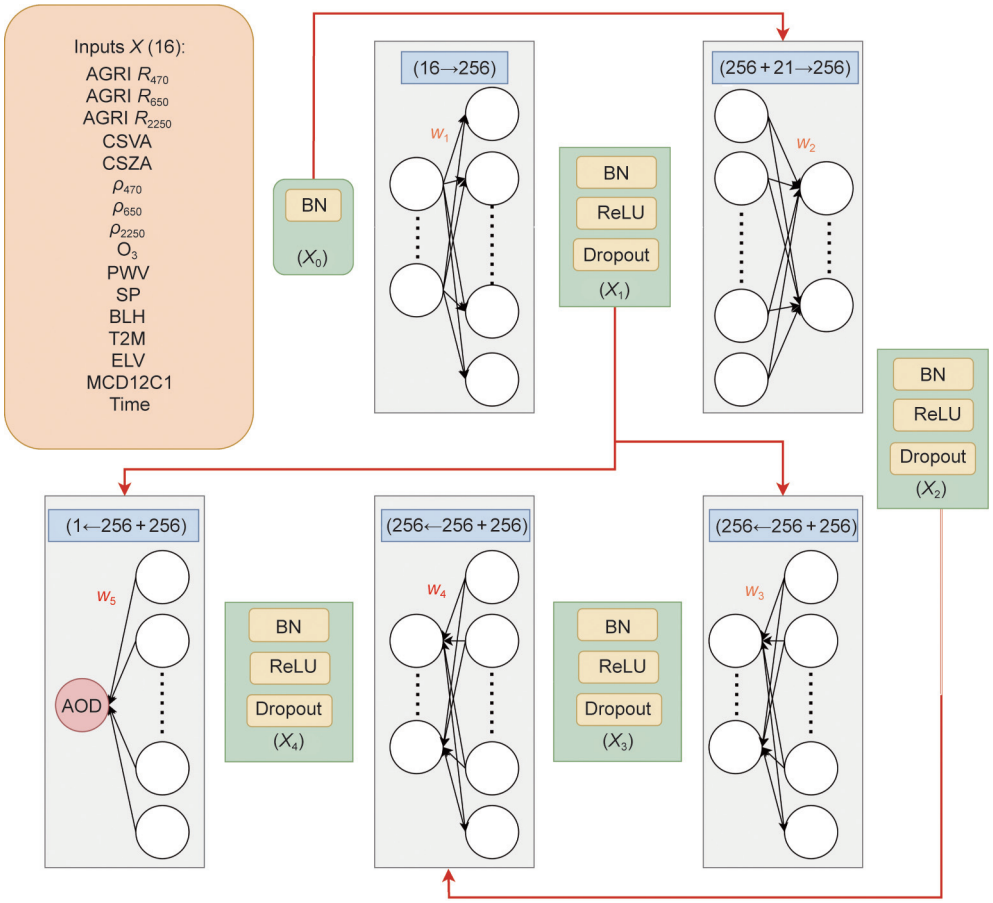

Fig. 2. Architecture of the hybrid model for advanced aerosol retrieval. Circles represent the input and output parameters of one layer, whereas red lines represent the skip connections. The coefficients w_i (i = 1, 2, . . ., 5) are the weight parameters of the neural network. The numbers in the blue boxes are the input and output dimensions of the network. The independent variables X_i (i = 0, 1, . . ., 4) refers to the inputs for each layer. BN: batch normalization.

connected layers of the pretrained network. In this study, the parameters in the front layers of the pretrained model are fixed as described in Section 3.3.2. The parameters of the full-connected layers (w_4 and w_5 in Fig. 2) are then adjusted by using the new target—that is, the sunphotometer AOD.

4. Results, verification, and discussion

4.1. Model performance in testing datasets and comparison among different methods

Here, two types of validation are used for both the baseline model development and the transfer-learning fine-tuning. First, according to the spatial distribution of the ground sites, 10% of the sites (90 out of 900 sample points and 9 out of 89 ground sites in Fig. S2) are evenly selected as the testing datasets (out-of-station validation). A ten fold cross validation is then used in the training process to learn the optimal hyper-parameters of the DNN. The parameters used to evaluate the model performance are R^2, the RMSE, the mean bias error (MBE), and the EE [58,59].

Fig. 3(a) shows the performance of the baseline model trained only with the AHI AOD at 90 AHI testing points. The results have a slight dispersion, with an R^2 of 0.63 and 59.4% of the predictions within the EE. The slope value of the linear regression is 0.82, indicating a slight underestimation, particularly when the aerosol loading is high. When the trained baseline model is directly applied to the nine testing sunphotometer sites (Fig. 3(b)), a slight degradation in model performance is observed (MBE increases from –0.01 to 0.06, and only 51.3% of the predictions remain within the EE). This suggests that the baseline model still has much room for improvement. Compared with Figs. 3(b) and (c) shows substantial improvement in the results of the model after fine-tuning, which suggests that the transfer-learning method has significantly improved the retrieval performance of the baseline model. More specifically, the fine-tuning approach increases R^2 to 0.70 and the slope to 0.91, while decreasing RMSE and MBE to 0.15 and 0.03, respectively. Moreover, 70.7% of the results are now within the EE.

Although the fine-tuning process does decrease both bias and random errors, Fig. 3(c) still displays significant scatter. Whereas this might be considered unavoidable to a large extent because of natural variability in the aerosol field, inadequacies in the retrieval procedure, and so forth, more scrutiny is warranted to help diagnose other possible sources of scatter. The comparisons in Fig. 3 are made between retrievals that represent an average AOD value over a satellite pixel and a point-source observation at a sunphotometric site located somewhere within that pixel. Here, the implicit assumption is thus that the ground-truth site is truly representative of the pixel in terms of the aerosol field. This is, however, not always the case in practice, such as wherever the ground-truth site is at a widely different elevation than the pixel's mean elevation. This situation particularly occurs when a ground-truth site is located at the bottom of a valley surrounded by high mountains or, conversely, located on top of an isolated high mountain surrounded by low-elevation terrain. For example, the latter case occurs with the Gaolanshan station, a top-of-mountain site

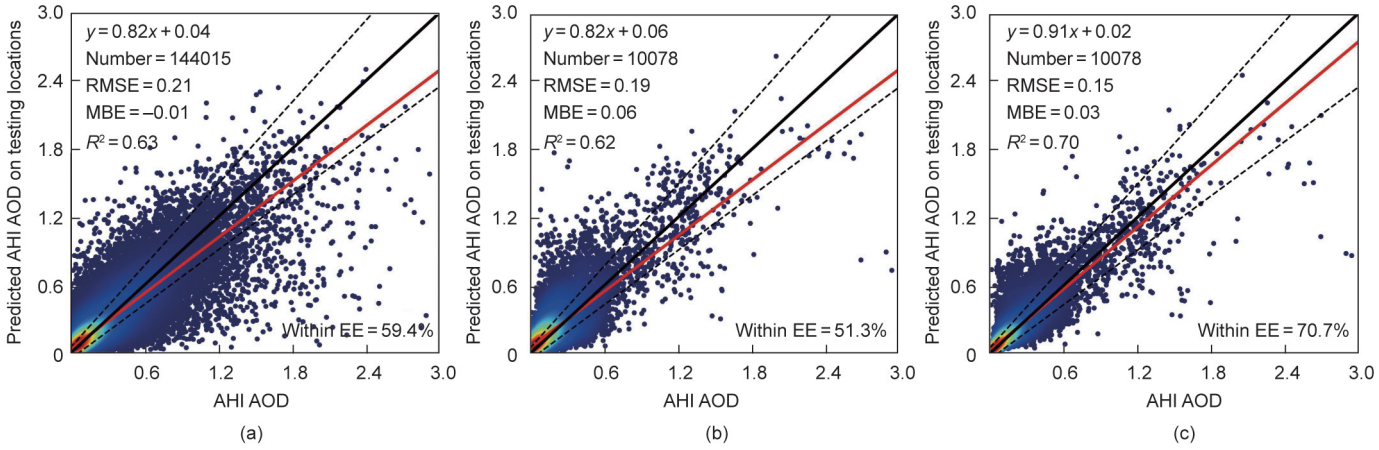

Fig. 3. Performance of the proposed hybrid AOD retrieval algorithm when considering (a) the baseline model (i.e., DNN with skip connections) at 90 testing AHI locations; (b) the baseline model at nine testing sunphotometer sites; (c) the fine-tuned model at nine testing sunphotometer sites. Solid black lines indicate the 1:1 diagonal, dashed lines represent the EE envelope.

at an elevation of 1668 m—that is, above most of the tropospheric aerosol layer. As a result, the observed reference AOD is much lower than the retrieved pixel's mean. Unfortunately, there is currently no specific criterion to evaluate the inherent heterogeneity of a pixel or to decide whether a ground-truth station should be excluded when conducting for this kind of validation. Arbitrarily removing such stations from the testing pool could lead to a loss of statistical significance and is therefore not an appropriate solution. Another approach would be to introduce a specific elevation correction to modify the retrieved AOD so that it becomes more directly comparable to the local ground truth. This is the process that was followed in Ref. [11], for example, but it is empirical and may not be ideal in all cases. Hence, it was not attempted here.

A comparison of the AGRI AOD retrieval results obtained here with those from previous studies is presented in Table 3 [36,37,60]. One difficulty is that the comparisons are made against different verification datasets or resolutions; hence, the validation results are not directly comparable on a fair basis. The MC method by Xie et al. [36] apparently performs best in terms of RMSE, percentage within the EE, and time resolution among the three studies reported here. Nonetheless, the MC method was originally applied over South Asia only, where aerosol properties are not more complex than those over China. Furthermore, the lower resolution 10 km AOD retrieved by Xie et al. [36] benefits from certain geographical smoothing effects, which tend to make the error smaller. The NNAeroG method by Ding et al. [37] achieves the best R^2, but it seems to underestimate at high AODs (slope = 0.71, intercept = 0.09). This underestimation can be expected, since only sunphotometer AODs are used as targets in NNAeroG, and any MSE loss would underestimate the rare occurrences (i.e., very high AODs). In comparison, the lowest RMSE (0.15), highest time/spatial resolution, and largest percentage of data within the EE (70.7%) are achieved by the present method. Furthermore, while the present R^2 of 0.70 is slightly lower than the first ranked value of 0.73 obtained by NNAeroG, the method proposed here largely solves the problem of underestimation with a self-defined loss function (slope = 0.91, intercept = 0.02). Overall, the results in Table 3 suggest that the current algorithm should be able to outperform the other three methods when verified against the same dataset at an identical spatiotemporal resolution.

4.2. Overview of AOD retrievals

Fig. S4 in Appendix A shows the mean AGRI AOD over the four seasons: March–April–May (MAM), June–July–August (JJA), September–October–November (SON), and December–January–February (DJF). The seasonal mean AGRI AOD values are 0.26, 0.22, 0.16, and 0.21 for the four seasons, respectively. A high AOD is the norm during MAM and JJA over the Tarim Basin because of the prevalence of desert dust then emitted by the Taklamakan Desert [44]. It should be noted that the AHI AOD cannot capture the high AOD over the Tarim Basin because the AHI's observation domain does not cover that region (Fig. S2(a)). High AOD values also occur over the North China Plain, where the occurrence of haze is typically frequent [61]. The lowest AOD values are observed over the Xizang Plateau because the high altitude of the Himalaya barrier prevents aerosol penetration from other regions, such as South Asia. The missing values in the north part of the figure for DJF are caused by the ice/snow cover, which prevents meaningful retrievals.

Numerous studies have shown that the MAIAC AOD product has high accuracy compared with ground-based sunphotometer AODs [9,62–64]. Therefore, the accuracy statistics between the seasonal mean MAIAC AOD and the AGRI AOD in the figure further demonstrate the reliability of the latter, with R^2 ranging from 0.50 to 0.68, a maximum MBE of less than 0.03, and at least 60.1% of the data within the EE.

Table 3
Overview of the performance of AOD retrievals from AGRI in published validation studies. The best value of each metric appears in boldface.

Method and author	Linear equation	RMSE	R^2	Percentage within EE	Time/spatial resolution	Study area	Source
MC	—	0.16	N/A	63.7%	5 min/10 km	South Asia (land)	[36]
DT-LUT	—	0.31	0.71	60% (EE20)	1 h/4 km	China (land)	[60]
NNAeroG	$y = 0.71x + 0.09$	0.24	0.73	58.7%	1 h/4 km	Full disk (land)	[37]
DNN with transfer learning	$y = 0.91x + 0.02$	0.15	0.70	70.7%	5 min/4 km	China (land and ocean)	This study

EE20 refers to the EE envelope of ±(0.05 + 20%) used by Jiang et al. [60]. x and y represent the satellite-derived AODs and the corresponding ground truths, respectively. NA: not available.

4.3. Extreme pollution event

An extreme aerosol case is selected here to demonstrate the advantages of the AGRI AOD under such conditions, which can be frequent in various parts of Asia. As shown in Fig. 4, the air quality in Beijing (one of the nine testing stations) on the afternoon of November 1, 2018 significantly deteriorated compared with the morning: the AOD increased from 0.09 at 00:50 to 0.52 at 07:45 (coordinated universal time (UTC), 8 h behind local time). However, the MAIAC AOD provides limited information, as only two AOD values are reported for that day (i.e., 0.19 at 02:30 and 0.24 at 05:30). Encouragingly, the AGRI AOD provides 33 observations for that day and reflects the continuous increase in AOD, reaching a maximum value of 0.44 in the afternoon. Remarkably, the AGRI AOD remains within ±0.1 of the ground-truth observations. The overestimation in the early hours is likely associated with the uncertainty in surface reflectance. As discussed in Section 3.2, the surface reflectance used in the present method is not strictly aerosol-free because not obtained by the usual atmospheric correction process. Hence, any underestimation in surface reflectance leads to an overestimation of the AGRI AOD.

In Fig. S5 in Appendix A, the AGRI AOD is overlaid with an red/green/blue (RGB) true-color image (also from AGRI) on November 1, 2018. The blue rectangle covering the Beijing–Tianjin–Hebei area is the region of interest (ROI). At 01:30 UTC, only about 50% of the ROI has an AOD value exceeding 0.4, with high values being concentrated in the southwest. Over time, the area with an AOD exceeding 0.4 within the ROI gradually increases, reaching nearly 75% of the ROI at 07:30 UTC. This gradual development process is not reflected by the MAIAC AOD because of its coarser temporal resolution. The three additional cases displayed in Fig. 5 also demonstrate the excellent results of the AGRI-based proposed method when applied to the monitoring of urban aerosols over areas where air pollution is variable and often significant, as in Beijing. The figure underlines that the present method can provide AOD retrievals that are comparable to the ground truth—and are often better than those of MAIAC—under low-, medium-, or high-AOD situations.

4.4. Feature contribution and uncertainty analysis

The Shapley additive explanations method proposed by Lundberg and Lee [65] is used here for model interpretability. This method assigns a contribution to each prediction feature by considering the marginal contribution of the feature when it is present. Table 4 displays the contributions of the top ten model features to the AGRI AOD retrievals. It is evident from the results that ELV (−0.23), R_{650} (−0.14), R_{470} (−0.13), and PWV (−0.12) are the four most important features (in terms of their absolute magnitude). Remarkably, higher values of these features correspond to smaller values of the AGRI AOD. A plausible explanation for this trend is that the high values of ELV are found over northwest China, where the AOD is relatively low. Regarding R_{650} and R_{470}, higher reflectance values in these two channels generally indicate less extinction of solar radiance by aerosols, thus lower AOD values. Moreover, relatively high PWV is commonly observed over the ocean, with extremely humid air wobbling north and south of the equator [66]. In contrast, high AOD values are closely associated with human activities over the land. Therefore, the negative contribution of PWV in the model likely reflects the difference in the respective spatial distributions of AOD and PWV. In contrast with the above four features, ρ_{650} exhibits a positive contribution (0.08), meaning that higher ρ_{650} values are associated with larger AODs. This explains why high values of both ρ_{650} and AOD always jointly appear over the Tarim Basin, as inferred from the surface reflectance in Fig. S3 and the seasonal mean AODs in Fig. S4.

According to the order of feature contributions in Table 4, sensitivity experiments are conducted for the top features. ELV is excluded here because of its high accuracy [68]. Therefore, only R_{650}, R_{470}, PWV, and ρ_{650} are selected for this sensitivity study. These specific variables are of obvious interest because the errors in sensors, reanalysis, and the surface reflectance proxy are expected to propagate down to the AOD retrieval. The benchmark of stimulation is extracted from the input features at the AERONET Beijing site on November 1, 2018. Specifically, R_{650} and R_{470} are the TOA reflectances from AGRI; PWV is derived from ERA5; ρ_{650} is the surface reflectance proxy at 650 nm. The uncertainties of R_{650} and R_{470} are all assumed to be 5%, as reported by Yang et al. [21]. The uncertainty of PWV is obtained from Wang et al. [67]. The uncertainty in ρ_{650} is calculated from the difference between the benchmark input value (0.09) and the AERONET average observation (0.10) at 02:00 on November 1, 2018. Table 5 summaries the sensitivity of the retrieved AOD to these features. As shown in the table, the largest error sources are R_{650} and R_{470}, whose relative errors in AOD retrievals vary from −18.88% to 10.43% and from −17.23% to 14.01%, respectively. The somewhat related ρ_{650} is the third largest source of error, as a consequence of the large relative uncertainty in ρ_{650} (±9%).

5. Conclusions

In this study, the AOD over land and ocean was estimated using a deep-learning and transfer-learning hybrid aerosol retrieval algorithm based on the AGRI sensor onboard the FY-4A geostationary satellite. This specific retrieval approach was chosen because a

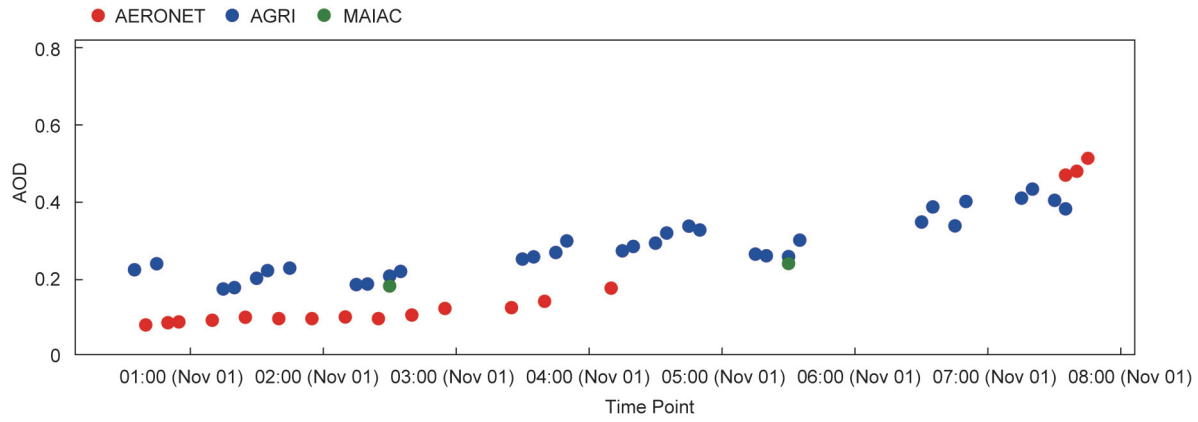

Fig 4. Variations of AERONET AOD, AGRI AOD, and MAIAC AOD over Beijing (116.38°E, 39.98°N) on November 1, 2018.

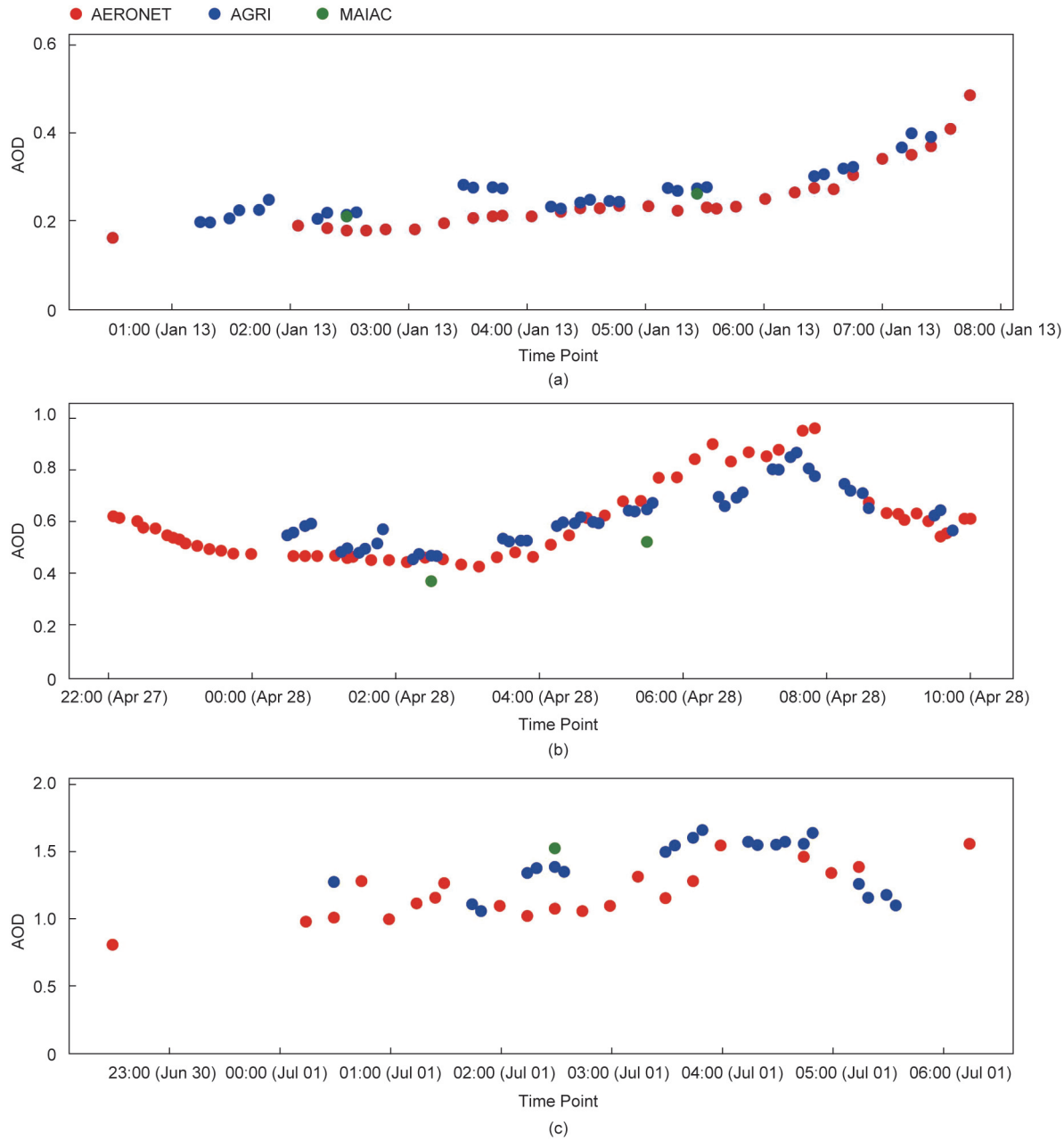

Fig. 5. Variations of AERONET AOD, AGRI AOD, and MAIAC AOD over Beijing (116.38°E, 39.98°N) on (a) January 13, 2018; (b) April 28, 2018; and (c) July 1, 2018.

Table 4
Feature contributions to the AGRI AOD retrieval (only the top 10 features are presented).

Feature name	Contribution
ELV	−0.23
R_{650}	−0.14
R_{470}	−0.13
PWV	−0.12
ρ_{650}	0.08
CSZA	0.08
ρ_{2250}	−0.05
R_{2250}	0.04
MCD12C1	−0.04
ρ_{470}	0.02

DNN requires large datasets to train network models, whereas the number of ground-based sunphotometer stations is limited. The proposed algorithm first uses 10 min AHI AODs as targets to train a baseline model (DNN with skip connections). Another core part of the hybrid algorithm is based on transfer learning, which, on top of the baseline model, uses sunphotometer AOD observations from 89 ground stations to fine-tune the parameters of the fully connected layer. The proposed algorithm ensures that sufficient samples exist to efficiently train the baseline model, and that the subsequent fine-tuning results in sufficient portability over the whole domain.

The algorithm was applied to a one year AGRI dataset for evaluation. Compared with the baseline model, employing transfer learning for fine-tuning was shown to substantially improve the model performance. The R^2 increased from 0.63 to 0.70, while the RMSE and MBE decreased from 0.19 and 0.06 to 0.15 and 0.03, respectively. Moreover, 70.7% of the results were found within the EE—an approximately 20% improvement over the baseline value of 51.3%. In applications where the AOD is needed to study extreme aerosol events, the present 5 min AGRI retrievals

Table 5
Sensitivity study for the input features of AGRI AOD retrievals.

Input feature	Benchmark input value	Assumed relative uncertainty in input (%)	Range of relative error in AOD retrieval (%)
R_{650}	0.09	±5	(−18.88, 10.43)
R_{470}	0.11	±5	(−17.23, 14.01)
PWV	9.39	±5	(−4.21, 4.07)
ρ_{650}	0.09	±9	(11.74, −10.80)

offer the important advantage of providing multiple AOD estimates during the day, at least in the absence of clouds over 4 km pixels. The feature importance study showed that the top five features contributing to AOD retrieval are ELV, R_{650}, R_{470}, PWV, and ρ_{650}. Considering the uncertainties and impacts of input features, R_{650}, R_{470}, and ρ_{650} were found to be the three largest error sources in the retrievals, followed by PWV. This study demonstrates the great potential of combining a physical approach with deep learning in geoscientific analysis. The proposed algorithm can also be applied to other multi-spectral sensors, such as AGRI on FY-4B.

Nevertheless, the present algorithm has still room for improvement. For example, the cloud detection method can affect the estimation of surface reflectance as well as the coverage of the retrieved AGRI AOD. More generally, the accuracy of aerosol retrieval techniques is closely tied to the exclusion of unsuitable pixels. Failure to accurately identify polluted layers as clouds or misclassifying clouds as polluted layers can lead to erroneous AOD estimates. These errors not only affect the overall quality of AOD products but also hinder the interpretation and utilization of remote-sensing data for various applications. Therefore, improvements to the cloud mask are being envisioned to improve the accuracy of the AGRI AOD in the future. Any other improvement in the determination of the surface reflectance at 650 nm would also be useful. If the proposed method is intended to be implemented operationally, the present reliance on the ERA5 reanalysis to obtain the input features poses a challenge due to its significant time delay. A possible alternative would be to obtain such data from a nowcast or forecast data stream provided by institutions such as CMA, ECMWF, or NOAA.

Moreover, the present method employed the AHI AOD as an intermediate target for the model. However, directly extracting its direct impact on the AGRI AOD is not a viable approach. To evaluate this impact, future investigations should consider utilizing two different versions of AHI AOD datasets. Furthermore, the present analysis focused on East Asia, where many sunphotometer stations exist. Further studies are needed to expand the validation to the whole FY-4A domain—that is, including other regions of Asia, Australia, and the oceans.

Acknowledgments

The work was supported by the National Natural Science of Foundation of China (41825011, 42030608, 42105128, and 42075079), the Opening Foundation of Key Laboratory of Atmospheric Sounding, the CMA and the CMA Research Center on Meteorological Observation Engineering Technology (U2021Z03). The AERONET and CARSNET staff and participants are thanked for their successful effort in establishing and maintaining the sites. The authors are grateful to the ECMWF for the reanalysis products, Japan Aerospace Exploration Agency for AHI AOD, and NASA for its MODIS products.

Compliance with ethics guidelines

Disong Fu, Hongrong Shi, Christian A. Gueymard, Dazhi Yang, Yu Zheng, Huizheng Che, Xuehua Fan, Xinlei Han, Lin Gao, Jianchun Bian, Minzheng Duan, and Xiangao Xia declare that they have no conflict of interest or financial conflicts to disclose.

Appendix A. Supplementary data

Supplementary data to this article can be found online at https://doi.org/10.1016/j.eng.2023.09.023.

References

[1] Forster P, Storelvmo T, Armour K, Collins W, Dufresne JL, Frame D, et al. The Earth's energy budget, climate feedbacks, and climate sensitivity. In: Masson-Delmotte V, Zhai P, Pirani A, Connors SL, Péan C, Berger S, editors. Climate change 2021: the physical science basis. Contribution of Working Group I to the Sixth Assessment Report of the Intergovernmental Panel on Climate Change. Cambridge: Cambridge University Press; 2021. p. 923–1054.
[2] Shi H, Yang D, Wang W, Fu D, Gao L, Zhang J, et al. First estimation of high-resolution solar photovoltaic resource maps over China with Fengyun-4A satellite and machine learning. Renew Sustain Energy Rev 2023;184:113549.
[3] Seinfeld JH, Bretherton C, Carslaw KS, Coe H, DeMott PJ, Dunlea EJ, et al. Improving our fundamental understanding of the role of aerosol–cloud interactions in the climate system. Proc Natl Acad Sci USA 2016;113(21):5781–90.
[4] Chudnovsky AA, Koutrakis P, Kloog I, Melly S, Nordio F, Lyapustin A, et al. Fine particulate matter predictions using high resolution aerosol optical depth (AOD) retrievals. Atmos Environ 2014;89:189–98.
[5] Che H, Xia X, Zhao H, Li L, Gui K, Zheng Y, et al. Aerosol optical and radiative properties and their environmental effects in China: a review. Earth-Science Rev 2024;248:104634.
[6] Butt EW, Rap A, Schmidt A, Scott CE, Pringle KJ, Reddington CL, et al. The impact of residential combustion emissions on atmospheric aerosol, human health, and climate. Atmos Chem Phys 2016;16(2):873–905.
[7] Bréon FM, Vermeulen A, Descloitres J. An evaluation of satellite aerosol products against sunphotometer measurements. Remote Sens Environ 2011;115(12):3102–11.
[8] de Leeuw G, Holzer-Popp T, Bevan S, Davies WH, Descloitres J, Grainger RG, et al. Evaluation of seven European aerosol optical depth retrieval algorithms for climate analysis. Remote Sens Environ 2015;162:295–315.
[9] Mhawish A, Sorek-Hamer M, Chatfield R, Banerjee T, Bilal M, Kumar M, et al. Aerosol characteristics from earth observation systems: a comprehensive investigation over South Asia (2000–2019). Remote Sens Environ 2021;259:112410.
[10] Xia X, Che H, Shi H, Chen H, Zhang X, Wang P, et al. Advances in sunphotometer-measured aerosol optical properties and related topics in China: impetus and perspectives. Atmos Res 2021;249:105286.
[11] Gueymard CA, Yang D. Worldwide validation of CAMS and MERRA-2 reanalysis aerosol optical depth products using 15 years of AERONET observations. Atmos Environ 2020;225:117216.
[12] Holben BN, Eck TF, Slutsker I, Tanré D, Buis JP, Setzer A, et al. AERONET—a federated instrument network and data archive for aerosol characterization. Remote Sens Environ 1998;66(1):1–16.
[13] Giles DM, Sinyuk A, Sorokin MG, Schafer JS, Smirnov A, Slutsker I, et al. Advancements in the Aerosol Robotic Network (AERONET) version 3 database—automated near-real-time quality control algorithm with improved cloud screening for sun photometer aerosol optical depth (AOD) measurements. Atmos Meas Tech 2019;12(1):169–209.
[14] Nakajima T, Campanelli M, Che H, Estellés V, Irie H, Kim SW, et al. An overview of and issues with sky radiometer technology and SKYNET. Atmos Meas Tech 2020;13(8):4195–218.
[15] Che H, Xia X, Zhao H, Dubovik O, Holben BN, Goloub P, et al. Spatial distribution of aerosol microphysical and optical properties and direct radiative effect from the China aerosol remote sensing network. Atmos Chem Phys 2019;19(18):11843–64.
[16] Xin J, Wang YY, Pan Y, Ji D, Liu Z, Wen T, et al. The campaign on atmospheric aerosol research network of China: CARE-China. Bull Am Meteorol Soc 2015;96(7):1137–55.
[17] Li ZQ, Xu H, Li KT, Li DH, Xie YS, Li L, et al. Comprehensive study of optical, physical, chemical, and radiative properties of total columnar atmospheric aerosols over China: an overview of Sun–Sky Radiometer Observation Network (SONET) measurements. Bull Am Meteorol Soc 2018;99(4):739–55.
[18] Schmetz J, Pili P, Tjemkes S, Just D, Kerkmann J, Rota S, et al. An introduction to Meteosat Second Generation (MSG). Bull Am Meteorol Soc 2002;83(7):977–92.
[19] Bessho K, Date K, Hayashi M, Ikeda A, Imai T, Inoue H, et al. An introduction to Himawari-8/9—Japan's new-generation geostationary meteorological satellites. J Meteorol Soc Jpn 2016;94(2):151–83.
[20] Choi H, Park S, Kang Y, Im J, Song S. Retrieval of hourly $PM_{2.5}$ using top-of-atmosphere reflectance from geostationary ocean color imagers I and II. Environ Pollut 2023;323:121169.
[21] Yang J, Zhang Z, Wei C, Lu F, Guo Q. Introducing the new generation of Chinese geostationary weather satellites, Fengyun-4. Bull Am Meteorol Soc 2017;98(8):1637–58.

[22] Zhang P, Zhu L, Tang S, Gao L, Chen L, Zheng W, et al. General comparison of FY-4A/AGRI with other GEO/LEO instruments and its potential and challenges in non-meteorological applications. Front Earth Sci 2019;6:224.
[23] Kaufman YJ, Tanré D, Remer LA, Vermote EF, Chu A, Holben BN. Operational remote sensing of tropospheric aerosol over land from EOS moderate resolution imaging spectroradiometer. J Geophys Res Atmos 1997;102(D14):17051–67.
[24] Hsu NC, Tsay S-C, King MD, Herman JR. Aerosol properties over bright-reflecting source regions. IEEE Trans Geosci Remote Sens 2004;42(3):557–69.
[25] Hsu NC, Jeong MJ, Bettenhausen C, Sayer AM, Hansell R, Seftor CS, et al. Enhanced Deep Blue aerosol retrieval algorithm: the second generation. J Geophys Res Atmos 2013;118(16):9296–315.
[26] Hsu NCC, Lee J, Sayer AMM, Carletta N, Chen SHH, Tucker CJJ, et al. Retrieving near-global aerosol loading over land and ocean from AVHRR. J Geophys Res Atmos 2017;122(18):9968–89.
[27] Lyapustin A, Wang Y, Laszlo I, Kahn R, Korkin S, Remer L, et al. Multiangle implementation of atmospheric correction (MAIAC): 2. aerosol algorithm. J Geophys Res Atmos 2011;116(D3):D03211.
[28] Dubovik O, Lapyonok T, Litvinov P, Herman M, Fuertes D, Ducos F, et al. GRASP: a versatile algorithm for characterizing the atmosphere [Internet]. Bellingham: SPIE Newsroom; 2019 Sep 19 [cited 2023 Oct 2]. Available from: https://spie.org/news/5558-grasp-a-versatile-algorithm-for-characterizing-the-atmosphere?SSO=1.
[29] NOAA NESDIS Center for Satellite Applications and Research (STAR). GOES-R Advanced Baseline Imager (ABI) algorithm theoretical basis document for suspended matter/aerosol optical depth and aerosol size parameter. 4th ed. Maryland: NOAA NESDIS Center for Satellite Applications and Research (STAR); 2018.
[30] Yoshida M, Kikuchi M, Nagao TM, Murakami H, Nomaki T, Higurashi A. Common retrieval of aerosol properties for imaging satellite sensors. J Meteor Soc Japan 2018;96B:193–209.
[31] She L, Zhang HK, Li Z, de Leeuw G, Huang B. Himawari-8 aerosol optical depth (AOD) retrieval using a deep neural network trained using AERONET observations. Remote Sens 2020;12(24):4125.
[32] Yeom JMM, Jeong S, Ha JSS, Lee KHH, Lee CSS, Park S. Estimation of the hourly aerosol optical depth from GOCI geostationary satellite data: deep neural network, machine learning, and physical models. IEEE Trans Geosci Remote Sens 2022;60:1–12.
[33] Kang Y, Kim M, Kang E, Cho D, Im J. Improved retrievals of aerosol optical depth and fine mode fraction from GOCI geostationary satellite data using machine learning over East Asia. ISPRS J Photogramm Remote Sens 2022;183:253–68.
[34] Chen X, De Leeuw G, Arola A, Liu S, Liu Y, Li Z, et al. Joint retrieval of the aerosol fine mode fraction and optical depth using MODIS spectral reflectance over northern and eastern China: artificial neural network method. Remote Sens Environ 2020;249:112006.
[35] Jiang X, Xue Y, Jin C, Bai R, Sun Y, Wu S. A simple Band Ratio Library (BRL) algorithm for retrieval of hourly aerosol optical depth using FY-4A AGRI geostationary satellite data. Remote Sens 2022;14(19):4861.
[36] Xie Y, Li Z, Guang J, Hou W, Salam A, Ali Z, et al. Aerosol optical depth retrieval over South Asia using FY-4A/AGRI data. IEEE Trans Geosci Remote Sens 2022;60:1–14.
[37] Ding H, Zhao L, Liu S, Chen X, de Leeuw G, Wang F, et al. FY-4A/AGRI aerosol optical depth retrieval capability test and validation based on NNAeroG. Remote Sens 2022;14(21):5591.
[38] Min M, Wu C, Li C, Liu H, Xu N, Wu X, et al. Developing the science product algorithm testbed for Chinese next-generation geostationary meteorological satellites: Fengyun-4 series. J Meteorol Res 2017;31(4):708–19.
[39] Cox C, Munk W. Measurement of the roughness of the sea surface from photographs of the Sun's glitter. J Opt Soc Am 1954;44(11):838–50.
[40] Hersbach H, Bell B, Berrisford P, Hirahara S, Horányi A, Muñoz-Sabater J, et al. The ERA5 global reanalysis. Q J Roy Meteor Soc 2020;146(730):1999–2049.
[41] Fu D, Gueymard CA, Yang D, Zheng Y, Xia X, Bian J. Improving aerosol optical depth retrievals from Himawari-8 with ensemble learning enhancement: validation over Asia. Atmos Res 2023;284:106624.
[42] Sulla-Menashe D, Friedl MA. User guide to collection 6 MODIS Land Cover Dynamics (MCD12Q2) product. Missoula: NASA EOSDIS L. Processes DAAC; 2018. p: 1–8.
[43] Bilal M, Nichol JE, Bleiweiss MP, Dubois D. A simplified high resolution MODIS aerosol retrieval algorithm (SARA) for use over mixed surfaces. Remote Sens Environ 2013;136:135–45.
[44] Su X, Wang L, Zhang M, Qin W, Bilal M. A High-precision aerosol retrieval algorithm (HiPARA) for Advanced Himawari Imager (AHI) data: development and verification. Remote Sens Environ 2021;253:112221.
[45] Chen Y, Fan M, Li M, Li Z, Tao J, Wang Z, et al. Himawari-8/AHI aerosol optical depth detection based on machine learning algorithm. Remote Sens 2022;14(13):2967.
[46] Hu Y, Liu L, Liu L, Peng D, Jiao Q, Zhang H. A landsat-5 atmospheric correction based on MODIS atmosphere products and 6s model. IEEE J Sel Top Appl Earth Obs Remote Sens 2014;7(5):1609–15.
[47] LeCun Y, Bengio Y, Hinton G. Deep learning. Nature 2015;521(7553):436–44.
[48] He K, Zhang X, Ren S, Sun J. Deep residual learning for image recognition. In: Proceedings of the 2016 IEEE Conference on Computer Vision and Pattern Recognition (CVPR 2016); 2016 Jun 27–30; Las Vegas, NV, USA. New York City: Institute of Electrical and Electronics Engineers (IEEE); 2016. p. 770–8.
[49] Weng W, Zhu X. U-Net: convolutional networks for biomedical image segmentation. IEEE Access 2021;9:16591–603.
[50] Drozdzal M, Vorontsov E, Chartrand G, Kadoury S, Pal C. The importance of skip connections in biomedical image segmentation. In: Proceedings of the International Workshop on Deep Learning in Medical Image Analysis (DLMIA 2016); 2016 Oct 21; Athens, Greece. Berlin: Springer; 2016. p. 179–87.
[51] Kingma DP, Ba JL. Adam: a method for stochastic optimization. arXiv 2014;1412:6980.
[52] Ren J, Zhang M, Yu C, Liu Z. Balanced MSE for imbalanced visual regression. In: Proceedings of the 2022 IEEE/CVF Conference on Computer Vision and Pattern Recognition (CVPR 2022); 2022 Jun 21–24; New Orleans, LA, USA. New York City: Institute of Electrical and Electronics Engineers (IEEE); 2022. p. 7916–25.
[53] Steininger M, Kobs K, Davidson P, Krause A, Hotho A. Density-based weighting for imbalanced regression. Mach Learn 2021;110(8):2187–211.
[54] Tan Y, Wang Q, Zhang Z. Assessing spatiotemporal variations of AOD in Japan based on Himawari-8 L3 V31 aerosol products: validations and applications. Atmos Pollut Res 2022;13(6):101439.
[55] Feng L, Su X, Wang L, Jiang T, Zhang M, Wu J, et al. Accuracy and error cause analysis, and recommendations for usage of Himawari-8 aerosol products over Asia and Oceania. Sci Total Environ 2021;796:148958.
[56] Yosinski J, Clune J, Bengio Y, Lipson H. How transferable are features in deep neural networks? Adv Neural Inf Process Syst 2014;4:3320–8.
[57] Liu Z, Yang Q, Shao J, Wang G, Liu H, Tang X, et al. Improving daily precipitation estimation in the data scarce area by merging rain gauge and TRMM data with a transfer learning framework. J Hydrol 2022;613:128455.
[58] Sayer AM, Munchak LA, Hsu NC, Levy RC, Bettenhausen C, Jeong MJ. MODIS collection 6 aerosol products: comparison between Aqua's e-deep blue, dark target, and "merged" data sets, and usage recommendations. J Geophys Res Atmos 2014;119(24):13965–89.
[59] Levy RC, Mattoo S, Munchak LA, Remer LA, Sayer AM, Patadia F, et al. The collection 6 MODIS aerosol products over land and ocean. Atmos Meas Tech 2013;6(11):2989–3034.
[60] Jiang X, Xue Y, Jin C, Bai R, Li N, Sun Y. Retrieval of aerosol optical depth over land using Fy-4Aagri geostationary satellite data. In: Proceedings of the 2021 IEEE International Geoscience and Remote Sensing Symposium IGARSS-2021; 2021 Jul 11–16; Brussels, Belgium. New York City: Institute of Electrical and Electronics Engineers (IEEE); 2021. p. 1931–4.
[61] Song Z, Fu D, Zhang X, Wu Y, Xia X, He J, et al. Diurnal and seasonal variability of $PM_{2.5}$ and AOD in North China Plain: comparison of MERRA-2 products and ground measurements. Atmos Environ 2018;191:70–8.
[62] Wang P, Tang Q, Zhu Y, Zheng K, Liang T, Yu Q, et al. Validation and analysis of MAIAC AOD aerosol products in East Asia from 2011 to 2020. Remote Sens 2022;14(22):5735.
[63] Mhawish A, Banerjee T, Sorek-Hamer M, Lyapustin A, Broday DM, Chatfield R. Comparison and evaluation of MODIS multi-angle implementation of atmospheric correction (MAIAC) aerosol product over South Asia. Remote Sens Environ 2019;224:12–28.
[64] Qin W, Fang H, Wang L, Wei J, Zhang M, Su X, et al. MODIS high-resolution MAIAC aerosol product: global validation and analysis. Atmos Environ 2021;264:118684.
[65] Lundberg SM, Lee SI. A unified approach to interpreting model predictions. In: Proceedings of the 31st International Conference on Neural Information Processing Systems (NeurIPS 2017); 2017 Dec 4–9; Long Beach, CA, USA. New York City: the Association for Computing Machinery; 2017. p. 4768–77.
[66] Chen B, Liu Z. Global water vapor variability and trend from the latest 36 year (1979 to 2014) data of ECMWF and NCEP reanalysis, radiosonde, GPS, and microwave satellite. J Geophys Res Atmos 2016;121(19):238.
[67] Wang S, Xu T, Nie W, Jiang C, Yang Y, Fang Z, et al. Evaluation of precipitable water vapor from five reanalysis products with ground-based GNSS observations. Remote Sens 2020;12(11):1817.
[68] Ibrahim M, Al-Mashaqbah A, Koch B, Datta P. An evaluation of available digital elevation models (DEMs) for geomorphological feature analysis. Environ Earth Sci 2020;79(13):336.